ARTICLE

Check for updates

Formation of organic color centers in air-suspended carbon nanotubes using vapor-phase reaction

Daichi Kozawa [1✉], Xiaojian Wu [2], Akihiro Ishii[1,3], Jacob Fortner[2], Keigo Otsuka [3], Rong Xiang [4,5], Taiki Inoue [5,6], Shigeo Maruyama [5], YuHuang Wang [2,7] & Yuichiro K. Kato [1,3✉]

Organic color centers in single-walled carbon nanotubes have demonstrated exceptional ability to generate single photons at room temperature in the telecom range. Combining the color centers with pristine air-suspended nanotubes would be desirable for improved performance, but all current synthetic methods occur in solution which makes them incompatible. Here we demonstrate the formation of color centers in air-suspended nanotubes using a vapor-phase reaction. Functionalization is directly verified by photoluminescence spectroscopy, with unambiguous statistics from more than a few thousand individual nanotubes. The color centers show strong diameter-dependent emission, which can be explained with a model for chemical reactivity considering strain along the tube curvature. We also estimate the defect density by comparing the experiments with simulations based on a one-dimensional exciton diffusion equation. Our results highlight the influence of the nanotube structure on vapor-phase reactivity and emission properties, providing guidelines for the development of high-performance near-infrared quantum light sources.

[1] Quantum Optoelectronics Research Team, RIKEN Center for Advanced Photonics, Saitama 351-0198, Japan. [2] Department of Chemistry and Biochemistry, University of Maryland, College Park, MD 20742, USA. [3] Nanoscale Quantum Photonics Laboratory, RIKEN Cluster for Pioneering Research, Saitama 351-0198, Japan. [4] State Key Laboratory of Fluid Power and Mechatronic Systems, School of Mechanical Engineering, Zhejiang University, Hangzhou 310027, China. [5] Department of Mechanical Engineering, The University of Tokyo, Tokyo 113-8656, Japan. [6] Department of Applied Physics, Osaka University, Osaka 565-0871, Japan. [7] Maryland NanoCenter, University of Maryland, College Park, MD 20742, USA. ✉email: daichi.kozawa@riken.jp; yuichiro.kato@riken.jp

Quantum technologies offer various advantages beyond the classical limits in secure communications[1], parallel computing[2], and sensing[3]. Solid-state single-photon sources[4] are a fundamental component in these technologies, and considerable progress has been made in various systems including quantum dots[5], diamond[6], SiC[7], and two-dimensional materials[8]. Of practical interest are single-walled carbon nanotubes (SWCNTs), since operation at room temperature and in the telecom range is possible. In particular, organic color centers formed on nanotubes[9] offer additional advantages with their optical properties being chemically tunable using a variety of molecular precursors, including aryl-halides[10–13], diazonium-salt[14–22], ozone[23–25], and hypochlorite[26] that can covalently bond to the carbon lattice. By introducing dopant states with different emission energies and achieving potential traps deeper than the thermal energy, single-photon sources with desired properties can be produced[27].

Further development of quantum emitters with improved performance is expected if color centers can be introduced to as-grown air-suspended SWCNTs known for their pristine nature[28,29]. In comparison to solution-processed tubes that have naturally formed quenching sites[30], the air-suspended nanotubes can be considered defect free except for the tube ends[28,29]. Such a system should provide an ideal platform for investigating photophysics of color centers[14,24], opening up new opportunities in nanoscale photonics using one- and zero-dimensional hybrid structures. Existing methods, however, require liquid-phase reactions where solvents and surfactants are inevitably in contact with the nanotubes, making the reactions incompatible with air-suspended nanotubes. To combine the excellent optical properties of the air-suspended SWCNTs with these organic color centers, an intelligent design of chemical reactions is needed.

In this work, we propose and demonstrate a vapor-phase reaction to create organic color centers in air-suspended SWCNTs. Tubes are functionalized with a photochemical reaction where adsorbing precursor vapor allows for preserving the suspended structures because of a weak mechanical perturbation. Individual tubes are characterized by confocal microspectroscopy to verify the formation of color centers, and we conduct a statistical survey of more than 2000 photoluminescence (PL) spectra to investigate diameter-dependent emission intensities and energies. PL intensity changes are interpreted using a theoretical model for reactivity that considers strain along the curvature of a SWCNT. We are also able to estimate the defect density by comparing experimentally obtained quenching with simulations based on numerical solutions of a diffusion equation. Characteristic trapping potential depths of color centers are studied by analyzing emission energies to elucidate the nature of the dopant states. Furthermore, we perform time-resolved PL measurements to investigate the dynamics of color center emission.

Results and discussion

PL spectroscopy for individual SWCNTs before and after the functionalization. Air-suspended SWCNTs are grown across trenches on Si substrates by chemical vapor deposition[31], and vapor-phase reaction using iodobenzene under ultraviolet (UV) irradiation is then conducted to create color centers. Figure 1a shows a schematic of a functionalized nanotube. Scanning electron microscopy confirms that the tubes stay suspended after the functionalization (Fig. 1b). We emphasize that the vapor-phase reaction here differs from typical functionalization techniques established for dispersed SWCNTs in liquid[10–13]. The solution process results in contaminating the tube surface and quenches PL due to interactions between SWCNTs and surrounding environment[32]. It is noteworthy that directly immersing tubes

into water inevitably destroys the air-suspended structures due to the high surface tension of the solvent (Supplementary Fig. 1).

We begin by examining PL spectra before and after the functionalization of a (10,5) SWCNT (Fig. 1c) by using the coordinates of the tube on the chip[31] to ensure that we are comparing the same individual tube. The pristine tube only shows exciton emission at a higher energy, whereas the functionalized tube shows two additional peaks at lower energies. We label the exciton emission at 1.02 eV as E_{11} and the additional peaks at 0.94 and 0.88 eV as E_{11}^- and E_{11}^{-*}, respectively. The lower energies of E_{11}^- and E_{11}^{-*} indicate that sp^3 defects of phenyl group are formed on SWCNTs which introduce dopant states[33]. No remarkable spectral shift of E_{11} emission peak is detected, suggesting negligible changes in dielectric environment due to the vapor residue. The overall PL intensity reduces to less than a quarter which implies introduction of quenching sites in addition to color centers. Hereafter, we refer to defects that decrease the E_{11} intensity as quenching sites and defects that give rise to the E_{11}^- and the E_{11}^{-*} peaks as color centers.

Imaging measurements are performed to characterize the spatial distributions of E_{11}, E_{11}^-, and E_{11}^{-*} emission. We scan over a (9,7) SWCNT to collect PL spectra and construct intensity maps for the three peaks by spectrally integrating intensities of each peak (Fig. 1d–f). The edges of the trench can be identified using a reflection image in the same area (Fig. 1g). Bright PL is emitted from the suspended region, as typically observed for air-suspended nanotubes[31]. The spatial profile of the E_{11} emission indicates the location of the nanotube and the additional peaks are observed along this tube, consistent with emission originating from color centers formed on the same tube. It is noted that E_{11}^- and E_{11}^{-*} emission show some spatial inhomogeneity in the intensity.

Statistical investigation of emission intensities. Emission from various chiralities are now studied by collecting PL spectra of more than 2000 individual SWCNTs before and after the functionalization. All PL data are obtained from a single substrate which assures that the reaction condition is the same, allowing for direct comparison among the chiralities. To acquire the data efficiently, we perform two sets of measurements with excitation energies of 1.46 and 1.59 eV which are near-resonant to many chiralities. Assuming that excitation is close to the E_{22} energy, chiralities of SWCNTs are assigned based on the E_{11} emission energy. For statistical analysis, 12 chiralities with sufficient numbers of tubes are used.

We first consider the intensity of E_{11} emission before the reaction. PL spectra are fitted by a Lorentzian function to obtain the spectrally integrated intensity I_0. Large dispersion is observed (Supplementary Figs. 12, 13, and 14), which can be attributed to various suspended lengths (Supplementary Note 1). Many SWCNTs are not fully suspended as observed in PL images (Supplementary Fig. 15), and their suspended lengths are likely shorter than the trench widths. Indeed, the intensity dispersion is well reproduced by simulations of length dependent PL intensity[28,29] assuming a log-normal length distribution[34] centered at 0.78 μm (Supplementary Fig. 16), indicating that most nanotubes have lengths ranging from 0.5 to 1.0 μm. We note that the simulations cannot be directly compared to experiments for nanotubes with no detectable PL, but the fraction of tubes is negligible at low intensities for the distribution reproducing the experimental data.

After the functionalization, color center emission appears in the PL spectra (Fig. 2a, b). All chiralities exhibit E_{11}^- and E_{11}^{-*} emission except for (10, 8), (11, 7), and (12, 5) SWCNTs whose E_{11}^{-*} is beyond the low energy detection limit. We find that most E_{11}^- peaks are taller than E_{11}^{-*} peaks.
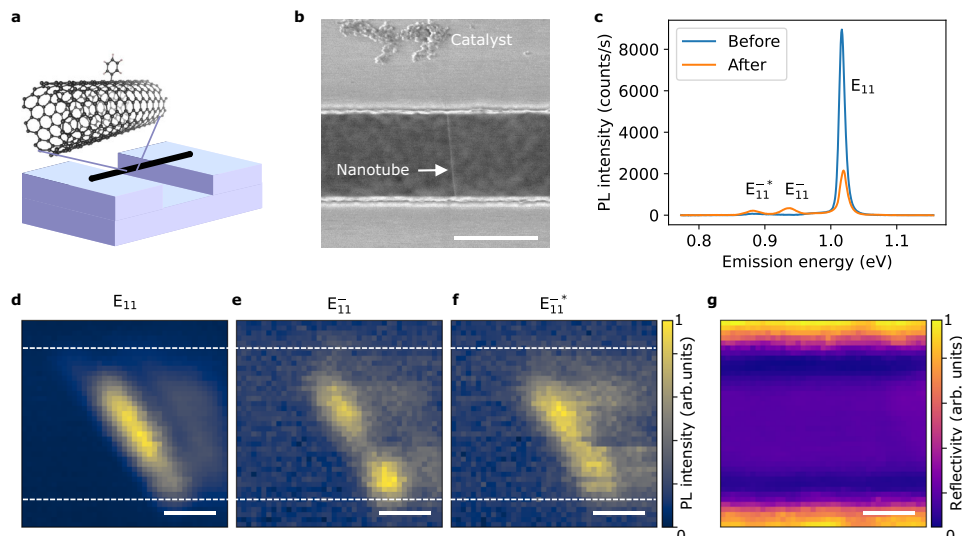
Fig. 1 Introducing organic color centers to air-suspended nanotubes using vapor-phase reaction. a A schematic of a functionalized SWCNT suspended across a trench on a Si substrate. **b** A scanning electron micrograph of a tube after the functionalization and the series of PL measurements. Particles on the top are patterned catalysts for growing SWCNTs and the nanotube is indicated by an arrow. **c** Representative PL spectra of an identical air-suspend (10,5) SWCNT before and after the functionalization taken with a laser power of 10 μW and an excitation energy of 1.59 eV. PL intensity maps of (**d**) E_{11}, (**e**) E_{11}^-, and (**f**) E_{11}^{-*} emission from a (9,7) tube where the intensity is integrated within a window of 37.4, 32.5, and 28.5 meV centered at each emission peak, respectively. The color scales are normalized to the maximum intensities in the respective maps. The dim features on the right of the tube are caused by reflection of the excitation laser from the bottom of the trench. The white broken lines indicate the edges of the trench. **g** A reflection image in the same area, where brighter and darker regions correspond to the surface of the substrate and the bottom of the trench, respectively. The scale bars in panels (**b**, **d–g**) are 1.0 μm. Source data for panels (**b–g**) are provided as a Source Data file.
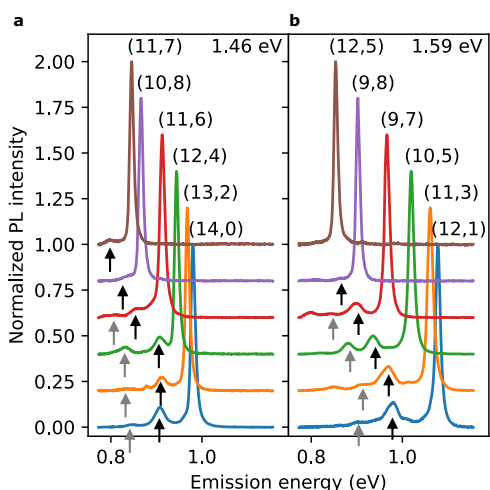

Fig. 2 Dopant state emission from various chiralities. PL spectra of functionalized SWCNTs collected with excitation laser energies of (**a**) 1.46 and (**b**) 1.59 eV and with an excitation power of 100 μW, where the spectra are displaced vertically for clarity. Black and gray arrows indicate E_{11}^- and E_{11}^{-*}, respectively. Chirality (n, m) is labeled next to the E_{11} peaks. Source data are provided as a Source Data file. Logscale PL spectra for each chirality are presented in Supplementary Fig. 2.

The intensity of E_{11}^- emission can be used to quantify color center density, but care must be taken because of the large variation in the emission intensity. We use the subpeak ratio I_{11}^-/I_{11} as a measure of the color center density, where I_{11}^- and I_{11} are the spectrally integrated intensities of E_{11}^- and E_{11} emission, respectively. By taking the ratio, the variations of E_{11} emission intensity can be canceled out to some degree. The subpeak ratio I_{11}^-/I_{11} is plotted as a function of E_{11} emission energy in Fig. 3 and for each chirality in Supplementary Fig. 3. We observe a

monotonically increasing trend with emission energy, indicating that smaller diameter tubes have more color centers (Supplementary Fig. 4). It should be noted that the chirality dependent E_{22} energy (Supplementary Fig. 5) results in emission intensity differences, since we fix the excitation energy either at 1.46 or 1.59 eV. Taking the ratio cancels out the chirality dependent E_{11} emission intensity, allowing for direct comparison between different chiralities. The intensity dispersion can also be caused by resonance shifts due to initial strain generated during growth and inhomogeneity of dielectric environment, but PL intensity variations should be insignificant since energy shifts are typically within ±10 meV[29]. Although small, the effects of these variations are likewise reduced by taking the ratio.

It is also possible to study the effects of the defects from the reduction of E_{11} emission due to the functionalization. In a manner similar to the subpeak ratio, we take the quenching degree $(I_0 - I_{11})/I_0$ as a more physically relevant quantity for comparison between different nanotubes with various suspended lengths and chiralities. The quenching degree exhibits an increasing trend with emission energy as in the case of I_{11}^-/I_{11} except for (9, 8) and (12, 5) nanotubes, which do not have a statistically sufficient number of data points (Fig. 3c, d). The large variation of the ratios (Supplementary Fig. 6) are likely caused by multiple factors including inhomogeneity among SWCNTs, temporal fluctuations in intensity (Supplementary Fig. 7), and positions of the defects[35]. We note that $(I_0 - I_{11})/I_0$ reflects the effects of color centers in addition to quenching sites, as both results in reduced E_{11} emission through trapping excitons.

A model for the chemical reactivity. To quantitatively interpret the trend of the subpeak ratio and the quenching degree, a theoretical model is developed. Chemical reactivity of SWCNTs depends on both π-orbital pyramidalization angle[36] and π-orbital misalignment angle between adjacent pairs of conjugated C atoms[18,37]. The former is subject to strain arising from the
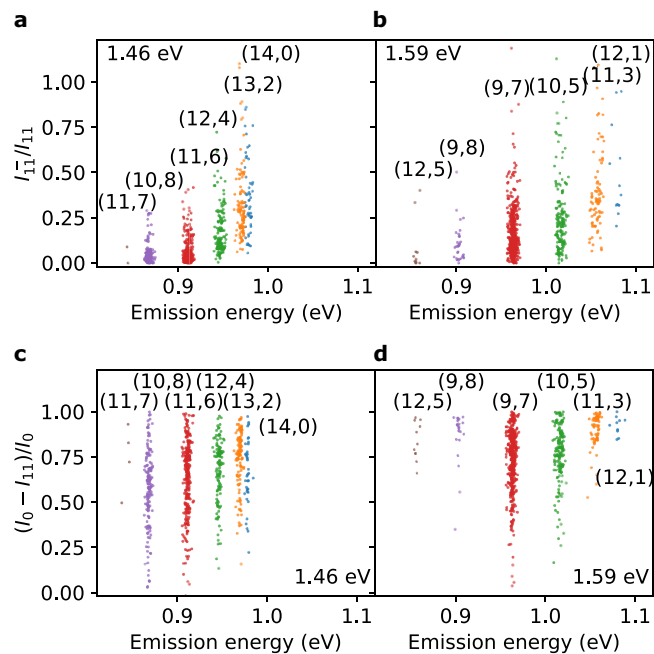
Fig. 3 Statistical analysis of PL intensities. Subpeak ratio I_{11}^-/I_{11} as a function of emission energy for experiments conducted with excitation energies of (**a**) 1.46 and (**b**) 1.59 eV and an excitation power of 100 μW. Quenching degree $(I_0 - I_{11})/I_0$ measured with excitation energies of (**c**) 1.46 and (**d**) 1.59 eV and an excitation power of 10 μW. Source data are provided as a Source Data file.

Fig. 4 Diameter-dependent reactivity. a A schematic defining the pyramidalization angle θ_p where $\mathbf{V}_\pi$ is a π-orbital axis vector, $\mathbf{V}_1$ is a unit vector pointing from the target atom to an adjacent atom[55]. The pyramidalization angle can be analytically estimated using a relationship $\cos(\theta_p + 90°) = \mathbf{V}_1 \cdot \mathbf{V}_\pi$. **b** Diameter dependence of computed pyramidalization angle, where the angles of armchair, zigzag, and chiral tubes are separately plotted. Diameter dependence of (**c**) subpeak ratio I_{11}^-/I_{11} and (**d**) quenching degree $(I_0 - I_{11})/I_0$, where error bars are the standard error of the mean. The solid line in panel (**b**) is a fit as explained in the main text, and the solid lines in panels (**c**, **d**) are fits by Eq. (1). **e** Simulations of E_{11} steady-state exciton density profile for no defects (blue), $\rho = 1.0$ (orange), and $\rho = 2.0$ μm^{-1} (green). The origin of the coordinate system is taken to be the center of the tube. **f** Diameter dependence of estimated defect density, where error bars are the standard error of the mean. The error bars in (**c**, **d**, **f**) are calculated from 5 to 53 measurements for each data point. Source data for panels (**b**–**f**) are provided as a Source Data file.

curvature of the tubular structure and is diameter dependent, whereas the latter originates from a bond angle with respect to the tube axis and is chiral angle dependent. As we observe a clear diameter dependence, our model considers the π-orbital pyramidalization angle θ_p depicted in Fig. 4a. The C–C bonds are more bent for larger θ_p, corresponding to larger strain. Figure 4b shows calculated pyramidalization angles as a function of the nanotube diameter d along with a fit by a scaling law $\theta_p = \delta/d$ where $\delta = 4.01°\,\mathrm{nm}^{-1}$ is the coefficient. Because the strain from the curvature increases the chemical reactivity[36], we assume that the reduction in the activation energy is proportional to the pyramidalization angle. The activation energy of the reaction is then $E_a(d) = E_a(\infty) - \eta\theta_p(d)$ where $E_a(\infty)$ is the activation energy for graphene, and η is the coefficient. According to the Arrhenius equation, it follows that the chemical reaction rates are proportional to

$$\exp\left(-\frac{E_a(\infty)}{k_B T} + \frac{1}{k_B T} \cdot \frac{\eta\delta}{d}\right) \qquad (1)$$

where k_B is the Boltzmann constant and $T = 298$ K is the temperature. The ratios I_{11}^-/I_{11} and $(I_0 - I_{11})/I_0$ should therefore scale as $\exp\left(\frac{1}{k_B T} \cdot \frac{\eta\delta}{d}\right)$.

Since data dispersion is large, we use the average values of these ratios for each tube diameter (Fig. 4c, d). We only include the tubes on the widest trenches with 3.0 μm width to reduce end quenching effects. It is confirmed that SWCNTs with smaller diameters show higher ratios, indicating that these tubes are more reactive despite the smaller surface areas. We fit the model to the experimental data, and both ratios show good agreement. The fit to I_{11}^-/I_{11} yields $\eta = 41.3 \pm 9.4$ meV/deg, whereas the fit to $(I_0 - I_{11})/I_0$ results in $\eta = 13.4 \pm 1.9$ meV/deg. The higher η for I_{11}^-/I_{11} by a factor of 3.08 indicates that the formation of color centers is more responsive to strain compared to quenching sites, although the higher excitation power used to obtain the subpeak
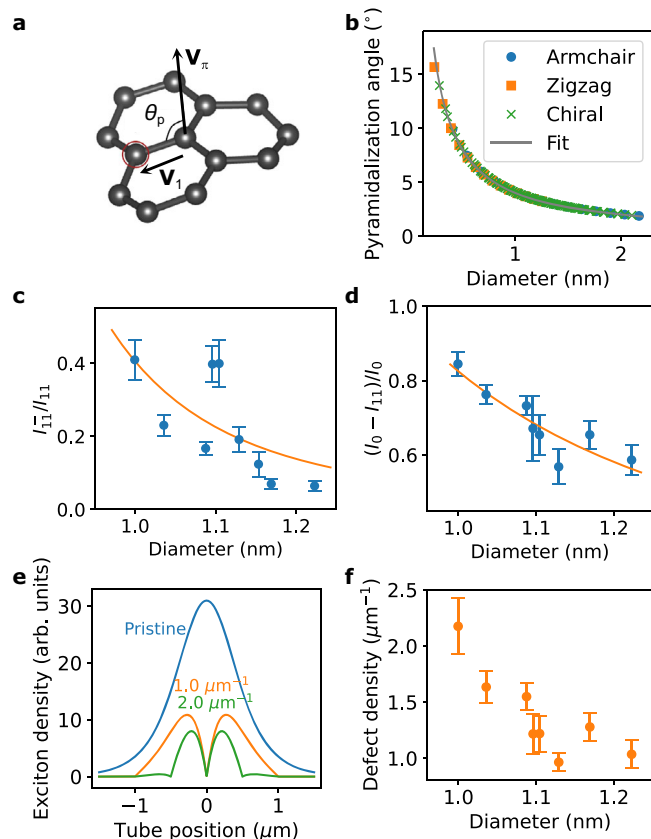
ratio could lead to underestimation of the reactivity for the color centers (Supplementary Fig. 18 and Note 2). It should be possible to use this difference for preferential creation of color centers by choosing tubes with smaller diameters. We note that an opposite diameter dependence on chemical reactivity has been reported for a reaction with 4-hydroxybenzene diazonium[38], where electron transfer limits the reaction rate.

Defect density estimation. The ratio $(I_0 - I_{11})/I_0$ also allows us to quantify the defect density by modeling the effects of functionalization on PL intensity. We use the fact that pristine air-suspended nanotubes are defect free except for end quenching[28,29]. Although the nanotubes used in this study have varying suspended lengths (Supplementary Note 1), the experimentally obtained distribution of I_0 (Supplementary Fig. 12) is consistent with a simulation assuming defect free nanotubes (Supplementary Fig. 16). In comparison, the experimental results

cannot be reproduced if initial defects are included in the simulations (Supplementary Fig. 17), and we therefore estimate the defect density in pristine SWCNTs to be much less than 0.25 μm^{-1}.

Our model is based on a steady-state one-dimensional diffusion equation

$$D\frac{d^2 n(z)}{dz^2} - \frac{n(z)}{\tau} + \frac{\Gamma_0}{\sqrt{2\pi r^2}}\exp\left(-\frac{z^2}{2r^2}\right) = 0 \qquad (2)$$

where D is the diffusion coefficient, $n(z)$ is the E_{11} exciton density, z is the position on the tube, $\tau = 70$ ps is the intrinsic lifetime of excitons[31], Γ_0 is the exciton generation rate, and $r = 530$ nm is the $1/e^2$ radius of the laser spot. The first term accounts for the exciton diffusion, the second term represents the intrinsic recombination, and the third term describes exciton generation which is proportional to the Gaussian laser profile. We consider SWCNTs with infinite length and set the boundary conditions to be $n(\pm\infty) = 0$. Additional boundary conditions $n(z_d) = 0$ are imposed for the functionalized tube where z_d is the position of defects, assuming that the sites are uniformly distributed with density ρ. For the diffusion coefficient, we use the expression $D = D_0(d/d_0)^\alpha$ where $D_0 = 15.36$ cm^2/s is the diffusion coefficient at diameter $d_0 = 1.00$ nm corresponding to a diffusion length $\sqrt{D\tau} = 328$ nm, and $\alpha = 2.56$ is the exponent[31]. The diffusion equation is numerically solved to obtain $n(z)$ and the results are plotted for various site densities in Fig. 4e (Supplementary Fig. 8a). When the defect separation is much shorter than the laser spot diameter, the quenching process becomes dominant over the intrinsic decay and results in a significant decrease in the exciton density.

The defect density is estimated by comparing $(I_0 - I_{11})/I_0$ obtained from the experiments with the simulations. We use the experimental data of tubes on the widest trenches with 3.0 μm widths, and the PL intensity in the simulation is computed by integrating $n(z)$ (Supplementary Fig. 8b). The only unknown parameter ρ is extracted by matching the simulated quenching degree with the experimental values. The results are plotted as a function of the diameter in Fig. 4f. The defect density ranges from 0.95 to 2.2 μm^{-1} and shows a diameter dependence which is consistent with the trend of the reactivity (Fig. 4c, d). The estimated defect density represents a lower bound because of the assumption in the simulations that defects are uniformly distributed in nanotubes (Supplementary Note 3). We also compare the distribution of $(I_0 - I_{11})/I_0$ between experiments and simulations (Supplementary Note 4). The experiments are well reproduced by a simulation assuming the log-normal length distribution and $\rho = 1.5$ μm^{-1} (Supplementary Figs. 19 and 20a). In comparison, a simulation with a high defect density of $\rho = 10$ μm^{-1} cannot reproduce the experimental results (Supplementary Fig. 20b). It is worth mentioning that the estimated defect density includes contributions from color centers and quenching sites as they both reduce the number of E_{11} excitons.

Emission energy analyses for various chiralities. We now proceed to analyze E_{11}^- and E_{11}^{-*} peak positions. Energy separations $\Delta E_{11}^- = E_{11} - E_{11}^-$ and $\Delta E_{11}^{-*} = E_{11} - E_{11}^{-*}$ can be interpreted as trapping potential depths for E_{11}^- and E_{11}^{-*} excitons, respectively, and we plot ΔE_{11}^- and ΔE_{11}^{-*} as a function of E_{11} in Fig. 5a, b. The energy separations show correlated increase with E_{11}, confirming that E_{11}^- and E_{11}^{-*} originate from dopant states of E_{11} exciton, and not of other states such as E_{22} and E_{33} excitons. It is noted that we observe smaller clusters for ΔE_{11}^- as marked by circles in Fig. 5a, whose trapping potentials are smaller than the main clusters. The differences in E_{11}^- could be assigned to different binding configurations of the phenyl functional group, where ortho- and para-configurations exhibit different emission energies[11,18,39]. We
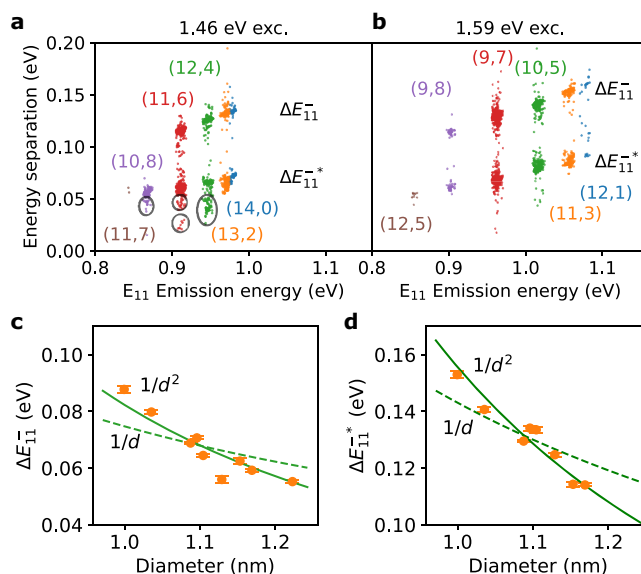

Fig. 5 Statistical analysis of emission energies. Energy separation ΔE_{11}^{-*} and ΔE_{11}^- of functionalized SWCNTs as a function of emission energy, where the data are collected with excitation energies of (**a**) 1.46 and (**b**) 1.59 eV and a power of 100 μW. The color of the dots represents the nanotube chirality and isolated clusters are indicated by circles. Diameter dependence of average (**c**) ΔE_{11}^- and (**d**) ΔE_{11}^{-*}, where error bars are the standard error of the mean and calculated from 25 to 373 measurements for each data point. The solid and broken lines are fits by the power laws $1/d^2$ and $1/d$, respectively. The data are better described by $\Delta E_{11}^- = A^-/d^2$ and $\Delta E_{11}^{-*} = A^{-*}/d^2$, where $A^- = 84.0 \pm 2.64$ meV·nm^2 and $A^{-*} = 154 \pm 1.43$ meV·nm^2 are the coefficients for ΔE_{11}^- and ΔE_{11}^{-*}, respectively. Source data are provided as a Source Data file.

similarly interpret the E_{11}^{-*} emission to be arising from other binding configurations.

The diameter dependence of the trapping potentials provides additional insight to the nature of the dopant states. The average values of ΔE_{11}^- and ΔE_{11}^{-*} for each chirality are plotted as a function of the diameter in Fig. 5c, d. The dependence shows a monotonic decrease and differs from the constant energy separation of 130 meV for the K-momentum excitons, and we thus exclude them from the origin of E_{11}^- and E_{11}^{-*}. To describe the dependence, we consider the $1/d$ scaling observed for the exciton binding energies and the $1/d^2$ scaling for singlet-triplet splitting[40–44] (Supplementary Note 5). The $1/d^2$ scaling yields better fits to both ΔE_{11}^- and ΔE_{11}^{-*} than the $1/d$ scaling.

The values of the energy separations ΔE_{11}^- and ΔE_{11}^{-*} observed in this work show more similarity to triplet[42,43] and trion states[45]. Examining the higher energy peak E_{11}^-, $\Delta E_{11}^- = 84.0$ meV at $d = 1$ nm is as high as the energy splitting reported for triplet excitons; Matsunaga et al. found $1/d^2$ dependence of energy separation for laser-induced defects in air-suspended SWCNTs[43], with a value of 70 meV at $d = 1$ nm. Nagatsu et al. showed the $1/d^2$-dependent energy separation in air-suspended SWCNTs for H_2-adsorption-induced peaks where $\Delta E_{11}^- = 68$ meV at $d = 1$ nm is attributed to triplet excitons[42]. The comparable values of the energies and the $1/d^2$ scaling for E_{11}^- suggest that the triplet exciton state is brightened at the color centers. Further study with optically detected magnetic resonance[46] and magneto-PL spectroscopy[47] would be required to clarify the triplet origin of E_{11}^- excitons. Considering the lower energy peak E_{11}^{-*}, $\Delta E_{11}^{-*} = 154$ meV at $d = 1$ nm is close to 175 meV-separation between exciton and trion energies for air-suspended SWCNTs[45] with a diameter of 1 nm. Using chemical[47] or electric-field[48] doping to investigate

trions trapped at color centers in air-suspended nanotubes may help elucidate the origin of the state. We note that the tubes studied here have larger diameters than typical SWCNTs dispersed in liquid[11,18], but the observed ΔE_{11}^- and ΔE_{11}^{-*} are consistent with the extrapolation of the d dependence for smaller diameters.

The diameter dependence of the trapping potential is partially responsible for the difference of subpeak ratio between air-suspended and solution-processed nanotubes[33]. The larger diameters for air-suspended SWCNTs lead to shallower trapping potentials[15,22], resulting in lower quantum yields for E_{11}^- emission. In addition, pristine air-suspended nanotubes can be considered defect free[28,29], whereas solution-processed tubes have naturally formed defects with a typical density of $8.3\,\mu m^{-1}$ [30]. I_0 in air-suspended nanotubes is therefore stronger than solution-processed tubes, further reducing the subpeak ratio.

The dynamics of excitons in a functionalized SWCNT. The dynamics of the color center emission is also investigated by time-resolved PL measurements to compare to the decay lifetimes of E_{11}. We use a pulsed laser for excitation, and the E_{11} emission is spectrally differentiated from the E_{11}^- and E_{11}^{-*} emission with a band-pass filter and a long-pass filter (Supplementary Fig. 9). Figure 6 shows PL decay curves for these emission peaks from an (11, 3) functionalized tube. Decay lifetimes are extracted by fitting a biexponential function $a_1 \exp(-t/\tau_1) + a_2 \exp(-t/\tau_2)$ convoluted with the instrument response function, where τ is the decay lifetime and a is the amplitude with the subscripts 1 and 2 denoting fast and slow components, respectively. We find that τ_1 for color center emission is 1.6 times longer than τ_1 for E_{11} exciton emission. This difference is moderate compared to 3.3 times observed for solution-processed SWCNTs[15] likely because of the lower defect density in air-suspended nanotubes resulting in longer E_{11} exciton lifetime.

The biexponential behavior for E_{11} and E_{11}^- emission is consistent with previous reports for solution-processed samples[15,22,49], where the decay for E_{11} can be understood by a three-level model including bright, dark, and ground states[50,51]. Both bright and dark excitons are populated by E_{22} resonant excitation and inter-state transitions take place between the bright and dark states, resulting in the fast component from bright
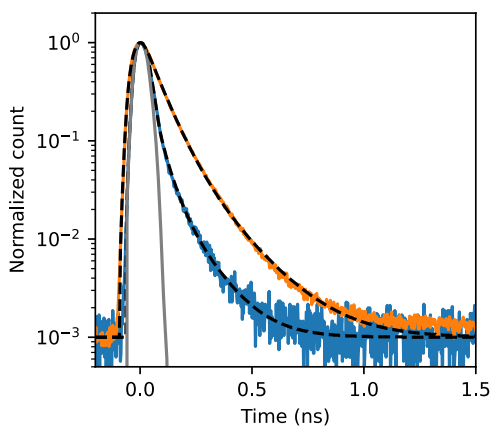
exciton recombination and the slow component reflecting the dynamics of dark excitons. The bixponential decay for color center emission can be similarly understood by considering an E_{11}^- manifold having three levels associated with the color center which is independent from the E_{11} states[15,23].

The lifetimes $\tau_1 = 69.1$ and $\tau_2 = 172.0$ ps for the color centers of the air-suspended nanotube are comparable to $\tau_1 = 86$ and $\tau_2 = 171$ ps for solution-processed tubes[15]. This result is reasonable because color centers are isolated and other defects should not affect the excitons trapped at the color centers. The comparable lifetimes also indicate that the vapor-phase reaction can form as high-quality color centers as the solution-processed methods. Although the diameter dependence of the potential depth for E_{11}^- exciton suggests its triplet nature, the observed lifetime is several orders of magnitude shorter than $30–200\,\mu s$ reported for the triplet states[46,52]. Lifetime shortening may be caused by hybridization of the singlet and triplet excitons[53].

Finally, we discuss how improvements can be made to take full advantage of the vapor-phase reaction. The formation of color center density can be adjusted by optimizing the duration of reaction time (Supplementary Fig. 10), ideally creating a single color-center per nanotube. We are aware of quenching sites introduced by UV irradiation itself, as observed in control experiments in the absence of iodobenzene (Supplementary Fig. 11). Suppression of this process could be possible by optimizing the power and the energy of UV light. By introducing deeper traps by different precursor molecules, quantum yield for E_{11}^- may be improved[22,33]. It is desirable to develop vapor-phase chemistry with these molecules for air-suspended nanotubes as the quantum yield in solution-processed nanotubes has improved by ~50% with a trapping potential deeper by 16 meV[22]. Because the potential depth depends on the diameter (Fig. 5c, d), SWCNTs with smaller diameters would be suited for higher quantum yield.

In summary, we have demonstrated functionalization of air-suspended SWCNTs using iodobenzene as a precursor. The comparison of PL spectra before and after the vapor-phase reaction shows additional peaks E_{11}^- and E_{11}^{-*} from color centers and PL intensity reduction of the E_{11} peaks. Twelve representative chiralities are characterized using spectra from more than 2000 individual tubes, where the diameter dependent subpeak ratio and quenching degree are observed. We have modeled the diameter dependent reactivity which is found to be proportional to $\exp(1/d)$, explaining the experimental results. By further performing the exciton diffusion simulations, we have estimated the defect density and found that these values are also diameter dependent. The analysis of peak energies reveals that both E_{11}^- and E_{11}^{-*} states originate from dopant states of E_{11} excitons and have trapping potentials scaling as $1/d^2$. We observe a longer PL lifetime for dopant states, similar to the reports on solution-processed tubes. By elucidating the exciton physics as well as functionalization chemistry, color centers in air-suspended SWCNTs should provide new opportunities in photonics and optoelectronics for quantum technologies.

Methods

Air-suspended carbon nanotubes. Electron-beam lithography and dry etching are used to fabricate trenches on Si substrates[54] with a depth of ~1 μm and a width of up to 3.0 μm. Another electron-beam lithography is conducted to define catalyst areas near trenches, and Fe-silica catalyst dispersed in ethanol are spin-coated and lifted off. SWCNTs are synthesized over trenches using alcohol chemical vapor deposition[31,54] under a flow of ethanol with a carrier gas of Ar/H₂ at 800 °C for 1 min.

Formation of organic color centers. Vapor-phase reaction is used to functionalize air-suspended nanotubes with iodobenzene as a precursor. As-grown SWCNTs on the Si substrates are placed facing up inside a glass chamber having a diameter of

Fig. 6 Time-resolved PL properties. PL decay curves of E_{11} emission (blue) and E_{11}^- and E_{11}^{-*} emission (orange) from a functionalized (11, 3) SWCNT suspended across a trench with a width of 1.0 μm measured by an excitation energy of 1.59 eV and a power of 10 nW using the pulsed laser. The broken lines are the fits by a biexponential decay function convoluted with the instrument response function (gray), showing $\tau_1 = 42.2$ and $\tau_2 = 122.0$ ps for E_{11} and $\tau_1 = 69.1$ and $\tau_2 = 172.0$ ps for E_{11}^- and E_{11}^{-*}. Source data are provided as a Source Data file.

15 mm and a height of 5 mm. Iodobenzene (5 μL) is introduced to the bottom of the chamber by a micropipette. The chamber is then covered with a quartz slide and sealed using high vacuum grease. We leave the chamber for 10 min to fill it with iodobenzene vapor, after which the reaction is triggered by irradiating the sample with 4.88-eV UV light through the quartz slide. The samples are collected from the chamber and stored in dark for characterization by subsequent spectroscopy.

Micro-PL measurements. PL spectra are obtained with a home-built scanning confocal microscope[31], where we use a continuous-wave Ti:sapphire laser for excitation and a liquid-N_2-cooled InGaAs photodiode array attached to a 30-cm spectrometer for detection. Laser polarization is kept perpendicular to trenches, and the beam is focused using an objective lens with a numerical aperture of 0.85 and a focal length of 1.8 mm. The $1/e^2$ diameters of the focused beams are 1.31 and 1.06 μm for excitation energies of 1.46 and 1.59 eV, respectively, where the diameters are characterized by performing PL line scans perpendicular to a suspended tube. PL excitation spectroscopy is conducted by scanning excitation wavelength at a constant power[29]. The reflected laser light is collected with a biased Si photodiode for reflection images. All PL spectra and decay curves are taken at the center of the nanotubes except for the hyperspectral PL imaging.

Spectral analysis. Peak parameters are extracted by fitting a Lorentzian function to PL spectra for pristine SWCNTs and a triple-Lorentzian function for functionalized SWCNTs. Pristine nanotubes with an E_{11} peak height of less than 500 counts/s are excluded in the statistics and not used for further measurements. We also exclude functionalized nanotubes with an E_{11} peak height of less than 400 counts/s.

Decay lifetime measurements. For time-resolved PL measurements, the Ti:sapphire laser is switched from continuous wave to ~100-fs pulses with a repetition rate of 76 MHz. A fiber-coupled superconducting single-photon detector is used to measure PL decay. Emission from E_{11} excitons and dopant states are separately obtained with a band pass filter and a long pass filter.

Data availability

References

1. Gisin, N. & Thew, R. Quantum communication. *Nat. Photonics* **1**, 165 (2007).
2. Di Ventra, M. & Pershin, Y. V. The parallel approach. *Nat. Phys.* **9**, 200 (2013).
3. Degen, C. L., Reinhard, F. & Cappellaro, P. Quantum sensing. *Rev. Mod. Phys.* **89**, 035002 (2017).
4. Aharonovich, I., Englund, D. & Toth, M. Solid-state single-photon emitters. *Nat. Photon.* **10**, 631 (2016).
5. Michler, P. et al. A quantum dot single-photon turnstile device. *Science* **290**, 2282 (2000).
6. Kurtsiefer, C., Mayer, S., Zarda, P. & Weinfurter, H. Stable solid-state source of single photons. *Phys. Rev. Lett.* **85**, 290 (2000).
7. Castelletto, S. et al. A silicon carbide room-temperature single-photon source. *Nat. Mater.* **13**, 151 (2014).
8. Tran, T. T., Bray, K., Ford, M. J., Toth, M. & Aharonovich, I. Quantum emission from hexagonal boron nitride monolayers. *Nat. Nanotech.* **11**, 37 (2016).
9. Brozena, A. H., Kim, M., Powell, L. R. & Wang, Y. Controlling the optical properties of carbon nanotubes with organic colour-centre quantum defects. *Nat. Rev. Chem.* **3**, 375 (2019).
10. Kim, M. et al. Mapping structure-property relationships of organic color centers. *Chem* **4**, 2180 (2018).
11. Gifford, B. J. et al. Optical effects of divalent functionalization of carbon nanotubes. *Chem. Mater.* **31**, 6950 (2019).
12. Wu, X., Kim, M., Kwon, H. & Wang, Y. Photochemical creation of fluorescent quantum defects in semiconducting carbon nanotube hosts. *Angew. Chem. Int. Ed.* **57**, 648 (2018).
13. Kwon, H. et al. Molecularly tunable fluorescent quantum defects. *J. Am. Chem. Soc.* **138**, 6878 (2016).
14. Iwamura, M. et al. Nonlinear photoluminescence spectroscopy of carbon nanotubes with localized exciton states. *ACS Nano* **8**, 11254 (2014).
15. Hartmann, N. F. et al. Photoluminescence dynamics of aryl sp^3 defect states in single-walled carbon nanotubes. *ACS Nano* **10**, 8355 (2016).
16. Akizuki, N., Aota, S., Mouri, S., Matsuda, K. & Miyauchi, Y. Efficient near-infrared up-conversion photoluminescence in carbon nanotubes. *Nat. Commun.* **6**, 1 (2015).
17. Ishii, A. et al. Enhanced single-photon emission from carbon-nanotube dopant states coupled to silicon microcavities. *Nano Lett.* **18**, 3873 (2018).
18. Saha, A. et al. Narrow-band single-photon emission through selective aryl functionalization of zigzag carbon nanotubes. *Nat. Chem.* **10**, 1089 (2018).
19. Luo, H. B., Wang, P., Wu, X., Qu, H., Ren, X. & Wang, Y. One-pot, large-scale synthesis of organic color center-tailored semiconducting carbon nanotubes. *ACS Nano* **13**, 8417 (2019).
20. Shiraki, T., Uchimura, S., Shiraishi, T., Onitsuka, H. & Nakashima, N. Near infrared photoluminescence modulation by defect site design using aryl isomers in locally functionalized single-walled carbon nanotubes. *Chem. Commun.* **53**, 12544 (2017).
21. Shiraki, T., Shiraishi, T., Juhász, G. & Nakashima, N. Emergence of new red-shifted carbon nanotube photoluminescence based on proximal doped-site design. *Sci. Rep.* **6**, 1 (2016).
22. Berger, F. J. et al. Brightening of long, polymer-wrapped carbon nanotubes by sp^3 functionalization in organic solvents. *ACS Nano* **13**, 9259 (2019).
23. Kim, M. et al. Fluorescent carbon nanotube defects manifest substantial vibrational reorganization. *J. Phys. Chem. C* **120**, 11268 (2016).
24. Miyauchi, Y., Iwamura, M., Mouri, S., Kawazoe, T., Ohtsu, M. & Matsuda, K. Brightening of excitons in carbon nanotubes on dimensionality modification. *Nat. Photon.* **7**, 715 (2013).
25. Ghosh, S., Bachilo, S. M., Simonette, R. A., Beckingham, K. M. & Weisman, R. B. Oxygen doping modifies near-infrared band gaps in fluorescent single-walled carbon nanotubes. *Science* **330**, 1656 (2010).
26. Lin, C.-W. et al. Creating fluorescent quantum defects in carbon nanotubes using hypochlorite and light. *Nat. Commun.* **10**, 2874 (2019).
27. He, X. et al. Tunable room-temperature single-photon emission at telecom wavelengths from sp^3 defects in carbon nanotubes. *Nat. Photon.* **11**, 577 (2017).
28. Moritsubo, S. et al. Exciton diffusion in air-suspended single-walled carbon nanotubes. *Phys. Rev. Lett.* **104**, 247402 (2010).
29. Ishii, A., Yoshida, M. & Kato, Y. K. Exciton diffusion, end quenching, and exciton-exciton annihilation in individual air-suspended carbon nanotubes. *Phys. Rev. B* **91**, 125427 (2015).
30. Hertel, T., Himmelein, S., Ackermann, T., Stich, D. & Crochet, J. Diffusion limited photoluminescence quantum yields in 1-D semiconductors: Single-wall carbon nanotubes. *ACS Nano* **4**, 7161 (2010).
31. Ishii, A., Machiya, H. & Kato, Y. K. High efficiency dark-to-bright exciton conversion in carbon nanotubes. *Phys. Rev. X* **9**, 041048 (2019).
32. Lefebvre, J., Homma, Y. & Finnie, P. Bright band gap photoluminescence from unprocessed single-walled carbon nanotubes. *Phys. Rev. Lett.* **90**, 217401 (2003).
33. Piao, Y. et al. Brightening of carbon nanotube photoluminescence through the incorporation of sp^3 defects. *Nat. Chem.* **5**, 840 (2013).
34. Wang, S., Liang, Z., Wang, B. & Zhang, C. Statistical characterization of single-wall carbon nanotube length distribution. *Nanotechnology* **17**, 634 (2006).
35. Harrah, D. M. & Swan, A. K. The role of length and defects on optical quantum efficiency and exciton decay dynamics in single-walled carbon nanotubes. *ACS Nano* **5**, 647 (2011).
36. Park, S., Srivastava, D. & Cho, K. Generalized chemical reactivity of curved surfaces: carbon nanotubes. *Nano Lett.* **3**, 1273 (2003).
37. Niyogi, S. et al. Chemistry of single-walled carbon nanotubes. *Acc. Chem. Res.* **35**, 1105 (2002).
38. Nair, N., Kim, W.-J. J., Usrey, M. L. & Strano, M. S. A structure-reactivity relationship for single walled carbon nanotubes reacting with 4-hydroxybenzene diazonium salt. *J. Am. Chem. Soc.* **129**, 3946 (2007).
39. He, X. et al. Low-temperature single carbon nanotube spectroscopy of sp^3 quantum defects. *ACS Nano* **11**, 10785 (2017).
40. Capaz, R. B., Spataru, C. D., Ismail-Beigi, S. & Louie, S. G. Diameter and chirality dependence of exciton properties in carbon nanotubes. *Phys. Rev. B* **74**, 121401(R) (2006).
41. Santos, S. M. et al. All-optical trion generation in single-walled carbon nanotubes. *Phys. Rev. Lett.* **107**, 187401 (2011).
42. Nagatsu, K., Chiashi, S., Konabe, S. & Homma, Y. Brightening of triplet dark excitons by atomic hydrogen adsorption in single-walled carbon nanotubes observed by photoluminescence spectroscopy. *Phys. Rev. Lett.* **105**, 157403 (2010).
43. Matsunaga, R., Matsuda, K. & Kanemitsu, Y. Origin of low-energy photoluminescence peaks in single carbon nanotubes: *K*-momentum dark excitons and triplet dark excitons. *Phys. Rev. B* **81**, 033401 (2010).
44. Palotás, J. et al. Incidence of quantum confinement on dark triplet excitons in carbon nanotubes. *ACS Nano* **14**, 11254 (2020).
45. Yoshida, M., Popert, A. & Kato, Y. K. Gate-voltage induced trions in suspended carbon nanotubes. *Phys. Rev. B* **93**, 041402(R) (2016).

46. Stich, D. et al. Triplet-triplet exciton dynamics in single-walled carbon nanotubes. *Nat. Photon.* **8**, 139 (2014).
47. Kwon, H. et al. Probing trions at chemically tailored trapping defects. *ACS Cent. Sci.* **5**, 1786 (2019).
48. Glückert, J. T. et al. Dipolar and charged localized excitons in carbon nanotubes. *Phys. Rev. B* **98**, 1 (2018).
49. He, X. et al. Solvent- and wavelength-dependent photoluminescence relaxation dynamics of carbon nanotube sp 3 defect states. *ACS Nano* **12**, 8060 (2018).
50. Gokus, T., Cognet, L., Duque, J. G., Pasquali, M., Hartschuh, A. & Lounis, B. Mono- and biexponential luminescence decays of individual single-walled carbon nanotubes. *J. Phys. Chem. C.* **114**, 14025 (2010).
51. Crochet, J. J., Duque, J. G., Werner, J. H., Lounis, B., Cognet, L. & Doorn, S. K. Disorder limited exciton transport in colloidal single-wall carbon nanotubes. *Nano Lett.* **12**, 5091 (2012).
52. Lin, C. W., Bachilo, S. M. & Weisman, R. B. Delayed fluorescence from carbon nanotubes through singlet oxygen-sensitized triplet excitons. *J. Am. Chem. Soc.* **142**, 21189 (2020).
53. Kim, Y. et al. Hidden fine structure of quantum defects revealed by single carbon nanotube magneto-photoluminescence. *ACS Nano* **14**, 3451 (2020).
54. Ishii, A., Uda, T. & Kato, Y. K. Room-temperature single-photon emission from micrometer-long air-suspended carbon nanotubes. *Phys. Rev. Appl.* **8**, 054039 (2017).
55. Haddon, R. C. Comment on the relationship of the pyramidalization angle at a conjugated carbon atom to the σ bond angles. *J. Phys. Chem. A* **105**, 4164 (2001).

Author contributions

Y.K.K., Y.H.W., and S.M. conceptualized the idea, and formulated the overarching research goals. A.I., T.I., and R.X. synthesized SWCNTs. X.W. and J.F. conducted the functionalization. D.K., A.I., and K.O. performed the optical measurements. D.K., A.I., and Y.K.K. interpreted the results. D.K. and Y.K.K. wrote the original draft with input from all the authors.

Competing interests

The authors declare no competing interests.

Additional information

Supplementary information The online version contains supplementary material available at https://doi.org/10.1038/s41467-022-30508-z.

Correspondence and requests for materials should be addressed to Daichi Kozawa or Yuichiro K. Kato.

Peer review information *Nature Communications* thanks the anonymous reviewers for their contribution to the peer review of this work. Peer reviewer reports are available.

Reprints and permission information is available at http://www.nature.com/reprints

Publisher's note Springer Nature remains neutral with regard to jurisdictional claims in published maps and institutional affiliations.